

Single-antenna 3D localization with nonseparable toroidal pulses

Ren Wang^{1,2*}, Pan-Yi Bao¹, Zhi-Qiang Hu¹, Bing-Zhong Wang¹ and Yijie Shen^{3,4*}

¹ Institute of Applied Physics, University of Electronic Science and Technology of China, Chengdu 611731, China

² Yangtze Delta Region Institute (Huzhou), University of Electronic Science and Technology of China, Huzhou 313098, China

³ Division of Physics and Applied Physics, School of Physical and Mathematical Sciences, Nanyang Technological University, Singapore 637378, Singapore

⁴ Centre for Disruptive Photonic Technologies, The Photonics Institute, Nanyang Technological University, Singapore 637378, Singapore

*Correspondence to: Ren Wang (rwang@uestc.edu.cn) and Yijie Shen (yijie.shen@ntu.edu.sg)

Abstract

The fundamental principle of satellite/node-based localization involves triangulating the receiver's localization by measuring distances between three or more known satellite/node localizations and receivers. Achieving accurate three-dimensional (3D) localization in free space based on a single transmission antenna remains a challenge requiring breakthroughs in principle. Here, we present such single-antenna 3D localization by applying a novel kind of topologically structured pulses, toroidal electromagnetic pulses, as information carriers. Excited by the recent compact generator of toroidal pulses and their sophisticated topological and nonseparable structures, we show that the space-time nonseparability and skyrmion topology of toroidal pulses can be utilized to achieve microwave 3D localization with super-resolution accuracy and experimentally validate its superior efficacy than the conventional triangulating microwave localization. This work opens up new avenues for exploring the potential applications of topological electromagnetic pulses including but not limited to positioning, imaging, and sensing technologies.

Keywords: toroidal pulses, space-time nonseparability, skyrmion topology, 3D localization

Introduction

Microwave-based wireless localization plays a crucial role in manufacturing, daily life, and scientific research [1-4]. Satellite navigation systems, such as the Global Positioning System (GPS), have revolutionized global navigation [5-7]. Recent advancements have led to the development of node network-based localization systems by replacing satellite transmitters with ground-based stations or network nodes, thereby enhancing the precision and adaptability of localization systems [8-11]. However, both node network-based and satellite-based localization systems rely on the multi-transmitter localization paradigm and spatial distance intersection technique, illustrated in Fig. 1(a), which entails high-precision ranging and synchronized distributed nodes, resulting in elevated system complexity and costs. Furthermore, achieving positioning accuracy at the wavelength scale necessitates synchronization precision at the

picosecond level, posing a significant challenge [1-11]. A promising approach to mitigate these challenges involves achieving receiver localization through a single transmitter node. The distributed multi-node system can be transformed into a centralized multi-element system [12], thereby reducing synchronization complexities among elements to a certain extent. Nevertheless, the underlying principle remains rooted in the spatial distance intersection of multi-transmitter localization paradigm.

The essence of the spatial distance intersection lies in comparing the differences in distance or electromagnetic wave propagation time/phase between different nodes or elements and the target to achieve localization. Consequently, exploiting multipath scattering enables the acquisition of information regarding the distance differences or electromagnetic wave propagation time/phase differences between different paths using single transmitter and single receiver [13,14]. Particularly, by reconfigurable intelligent surfaces to control multipath scattering, it is even possible to achieve super-resolution precise localization based on single transmission antenna [15,16]. However, in free space where multipath scattering is unavailable for exploitation, achieving accurate three-dimensional (3D) localization based on a single transmission antenna remains a challenge requiring breakthroughs in principle.

Topological electromagnetic fields exhibit vast potential applications in information and energy transmission [17-23] and super-resolution metrology or microscopy [24-29], thereby offering a potential avenue for achieving precise 3D localization based on a single transmission antenna in free space. In 1996, Hellwarth and Nouchi introduced toroidal pulses, an exact solution to Maxwell's equations [30], which possess complex non-transverse skyrmion topological structures [31-34], space-time nonseparability [35-38], and strong interactions with matter [39,40]. Recently, electromagnetic toroidal pulses have been successfully generated in the optics, terahertz, and microwave [41-43], laying the foundation for their practical applications. However, there have been no reports of successful experimental implementations of toroidal pulses until now.

In this paper, we break through the spatial distance intersection based free-space localization paradigm and present a novel method for 3D localization based on the space-time nonseparability and skyrmion topology of toroidal pulses. Our method enables 3D spatial localization with super-resolution accuracy using a single microwave toroidal pulse transmission antenna. The effectiveness of this method is validated through both theoretical analysis and experimental verification. As a result, the proposed methodology utilizing toroidal pulses paves the way for the establishment of novel, straightforward, and highly efficient 3D localization systems.

Results

Localization principle based on nonseparable toroidal pulses. The space-time nonseparability and space-polarization nonseparability of toroidal pulses, evident in their analytical expressions, are the fundamental principles underlying the proposed 3D localization method. The expression for the field distribution of transverse-magnetic (TM) toroidal pulses (Figs. 1(b1 and b2)) in a cylindrical coordinate system is as follows [30]:

$$H_{\theta} = 4if_0 \frac{\rho(q_1+q_2-2ict)}{[\rho^2+(q_1+i\tau)(q_2-i\sigma)]^3} \quad (1)$$

$$E_{\rho} = 4if_0 \sqrt{\frac{\mu_0}{\varepsilon_0}} \frac{\rho(-q_1+q_2-2iz)}{[\rho^2+(q_1+i\tau)(q_2-i\sigma)]^3} \quad (2)$$

$$E_z = -4f_0 \sqrt{\frac{\mu_0}{\varepsilon_0}} \frac{\rho^2-(q_1+i\tau)(q_2-i\sigma)}{[\rho^2+(q_1+i\tau)(q_2-i\sigma)]^3} \quad (3)$$

where, H_{θ} is the magnetic field component in the θ direction, E_{ρ} and E_z are the electric field components in the ρ and z directions, respectively. The i denotes the imaginary unit, f_0 represents a real constant, q_1 and q_2 are adjustable real positive parameters, c represents the speed of light, t denotes time, $\tau = z - ct$, $\sigma = z + ct$. μ_0 and ε_0 represent the permeability and permittivity in vacuum, respectively.

Due to the inability to separate the spatial variable ρ from the temporal variable t in the expression of toroidal pulses mentioned above, their field equations cannot be expressed as spatial field forms with the temporal variable eliminated or temporal field forms with the spatial variable eliminated. This unique characteristic is referred to as space-time nonseparability, which is equivalent to space-frequency nonseparability. Due to their space-time nonseparability, toroidal pulses exhibit distinct electromagnetic fields in both the temporal and frequency domains at each spatial location [37]. When examining the maximum field distribution of toroidal pulses at a specific frequency point as it varies with the propagation space, we obtain a distribution of maximum spectral lines as shown in Fig. 1(b3). The solid lines represent the radial maximum values of the E_ρ component along the z -axis for several frequencies ranging from f_{\max} to f_{\min} , with decreasing frequency from the inner to the outer regions. The maximum spectral lines are mutually separated and never intersect, which is one manifestation of the space-time nonseparability of toroidal pulses [37]. This spatial-frequency correspondence forms the foundation for localization based on the space-time nonseparability. The correspondence between spatial and frequency spectra enables the determination of target coordinates (ρ, z) . For further details, please refer to the supplementary material.

Drawing inspiration from animals that navigate using electromagnetic wave polarization [44,45], we can also utilize the polarization properties of toroidal fields for localization purposes. Toroidal fields exhibit space-polarization nonseparability apart from space-time nonseparability [31-34], with their skyrmion polarization textures having been experimentally observed [43]. This intricate spatial topological feature holds the potential for achieving ultrahigh resolution localization. Taking TM toroidal pulses as an example, E_ρ exhibits skyrmion-type polarization, as indicated in Fig. 1(b4). The azimuthal coordinate θ of the target can be determined based on the polarization characteristics of the electric field vector. Consequently, the time/frequency-polarization information at each 3D spatial point within the primary distribution region of the toroidal field is unique, meaning that it can be uniquely characterized by the time-polarization state or frequency-polarization state. As shown in Fig. 1, by discretizing the 3D space into a grid and placing receivers at each grid point, we can measure the time/frequency-polarization state at each point and store it

along with the corresponding spatial coordinates as a localization information database. Subsequently, by measuring the time/frequency-polarization state at any target spatial point and comparing it with the localization information database, we can obtain the corresponding spatial coordinates, thus achieving target localization.

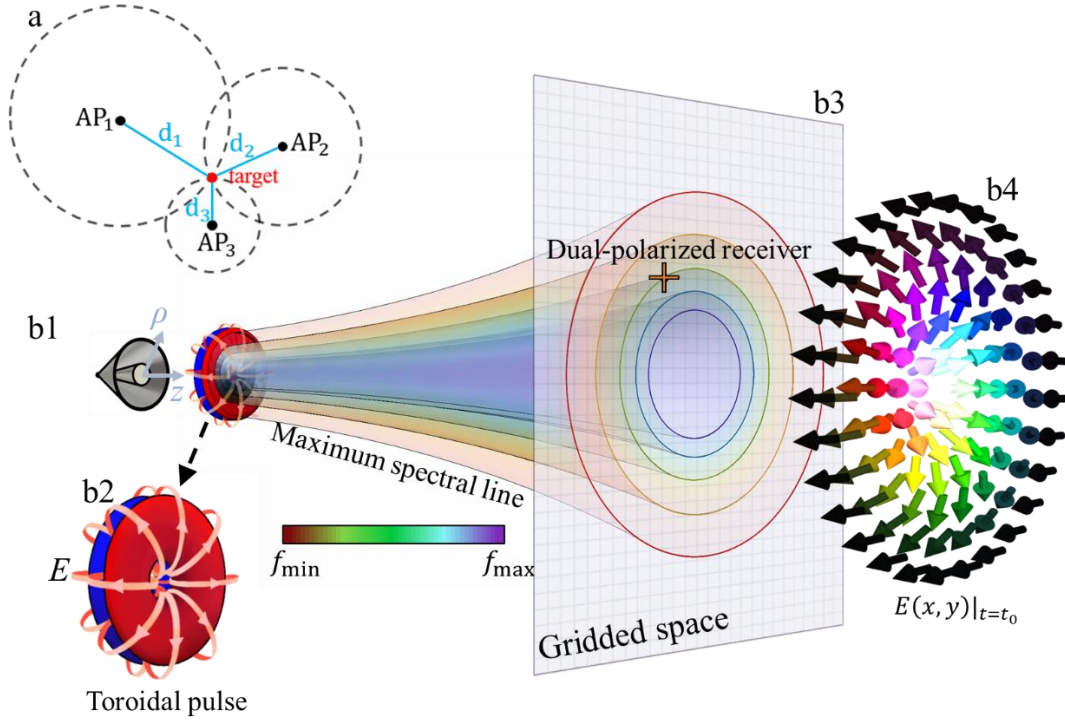


Fig. 1 Schematic diagram of 3D localization method based on toroidal pulses. (a) Traditional spatial distance intersection principle, where AP represents access point; (b1) Toroidal pulses emission antenna; (b2) Electric field distribution of TM toroidal pulses, with the electric field E indicated by encircling pink arrows; (b3) Schematic diagram of the maximum frequency localization and polarization distribution of toroidal pulses. We annotate the maximum localization of the single-frequency field distribution in the ρ direction (referred to as the maximum spectrum line) using solid lines of different colors (from violet to red indicating from high to low frequencies). After spatial discretization, the maximum spectrum lines intersect with circular coils on a plane perpendicular to the propagation axis (z -axis). (b4) Skyrmion topology in toroidal pulses.

Single-antenna 3D localization performances. Shen et al. introduced the space and time states as a set of entangled states based on the spatial and temporal properties of toroidal pulses [37]. These states were quantized through measurements of the state density matrix to assess the spatiotemporal inseparability of the toroidal pulses. Inspired by this approach, we define the frequency-polarization amplitude state $|\psi_a\rangle$ and the phase state $|\psi_p\rangle$, leveraging the unique frequency-polarization information at each localization within the propagation space of the toroidal pulses.

$$|\psi_a\rangle = [|E_{hor}(\lambda, \rho, z, \theta)|, |E_{ver}(\lambda, \rho, z, \theta)|] \quad (4)$$

$$|\psi_p\rangle = [\arctan\left(\frac{\text{Im}(E_{hor}(\lambda, \rho, z, \theta))}{\text{Re}(E_{hor}(\lambda, \rho, z, \theta))}\right), \arctan\left(\frac{\text{Im}(E_{ver}(\lambda, \rho, z, \theta))}{\text{Re}(E_{ver}(\lambda, \rho, z, \theta))}\right)] \quad (5)$$

where, E_{hor} and E_{ver} denote the horizontal and vertical components of the normalized transverse electric field of the toroidal pulses, respectively. We exploit the regularity of the spatial field distribution of the toroidal pulses through measurements of the amplitude of the electric field, and the regularity of its spatial polarization by measuring the phase angles of the electric field components in different directions. Specifically, the frequency-polarization amplitude state encodes information about spatial distance and radial localization, while the frequency-polarization phase state contains information about the spatial azimuthal localization. Drawing inspiration from the concept of fidelity in quantum mechanics, we introduce a spatial pseudo-spectrum tailored for receiver localization.

$$F_{tol} = F_a * F_p \quad (6)$$

$$F_a = \frac{\langle \psi_{a,tar} | \psi_{a,pre} \rangle \langle \psi_{a,tar} | \psi_{a,pre} \rangle}{\langle \psi_{a,tar} | \psi_{a,tar} \rangle \langle \psi_{a,pre} | \psi_{a,pre} \rangle} \quad (7)$$

$$F_p = \frac{\langle \psi_{p,tar} | \psi_{p,pre} \rangle \langle \psi_{p,tar} | \psi_{p,pre} \rangle}{\langle \psi_{p,tar} | \psi_{p,tar} \rangle \langle \psi_{p,pre} | \psi_{p,pre} \rangle} \quad (8)$$

where, the subscript "tar" represents the frequency-polarization state measured by the receiver at the target location, while the subscript "pre" denotes the frequency-polarization state obtained from a pre-measured localization information database at different positions within the area of interest. In Eqs. (6-8), both F and $|\psi_{pre}\rangle$ are functions of the coordinate localization (ρ, z, θ) , while $|\psi_{tar}\rangle$ is computed based on the signals received by the receiver at the location (ρ_0, z_0, θ_0) . Consequently, the computation of F_{tol} using the aforementioned equations yields pseudo-spectrum values for different localizations (ρ, z, θ) , as illustrated in Fig. 2. In Fig. 2, the target is situated at $(x, y, z) = (0, 0.1, 0.2)$ m, with the toroidal pulses propagating in the z -direction, and the frequency range used for computing the pseudo-spectrum is 2-10 GHz.

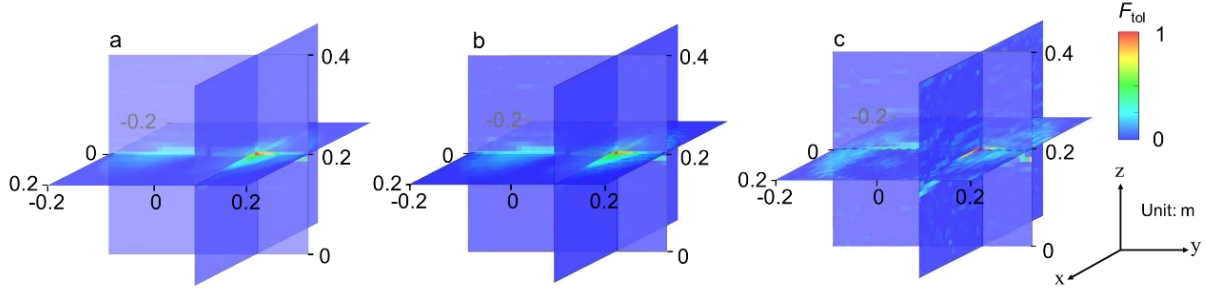


Fig. 2 Three-dimensional localization pseudo-spectrum based on toroidal pulses. (a) Ideal toroidal pulse-based localization pseudo-spectrum; (b) Localization pseudo-spectrum computed with toroidal pulses at a signal-to-noise ratio of 20 dB; (c) Experimental localization pseudo-spectrum constructed from measured data. The target is located at $(x, y, z) = (0, 0.1, 0.2)$ m, with the toroidal pulses propagating in the z -direction and their cross-sectional center located at $(x = 0, y = 0)$.

Fig. 2(a) depicts the pseudo-spectrum computed using ideal toroidal pulses (given by Eqs. (1-3) with $q_1=0.02\text{m}$ and $q_2=50q_1$). It is evident from the figure that the spatial coordinate corresponding to the maximum pseudo-spectrum value, i.e. 1, aligns with the target location, with high pseudo-spectrum values observed near the target and low values at distant locations. This clearly indicates the target's localization. In practical localization applications, however, test errors due to noise are inevitable. To assess the performance of our method in noisy conditions, we superimposed Gaussian white noise with a signal-to-

noise ratio of 20 dB on the ideal toroidal pulses field at each localization. The recomputed pseudo-spectrum is shown in Fig. 2(b), which exhibits similar results to Fig. 2(a), indicating a degree of noise robustness. To validate the localization method proposed in this study, we conducted experimental tests using a coaxial horn toroidal pulses transmission antenna (Fig. 1(b1)), as described in [43]. Experimental settings are detailed in the Method. The measured 3D pseudo-spectrum is presented in Fig. 2(c), clearly identifying the target's location in the experimental results, agreeing well with theoretical predictions.

As observed in Fig. 2, although the maximum value of F_{tol} in the pseudo-spectrum indicates the target's localization, the relatively high values of F_{tol} in the vicinity of the target can potentially affect the method's resolution. To improve the purity of the pseudo-spectrum and enhance resolution without compromising localization accuracy, we can employ techniques to sharpen the pseudo-spectrum. These techniques are described in detail in the Supplementary Material.

Simultaneous localization of multiple receivers. Beyond the localization of a single receiver, our method also enables the simultaneous localization of multiple receivers situated at different locations. By separately computing pseudo-spectra using signals received by different receivers and superimposing the sharpened pseudo-spectra, we can obtain a pseudo-spectrum map for multi-target localization. Since the sharpened pseudo-spectrum values outside the target localizations are very small, the superimposed localization of pseudo-spectra corresponding to individual receivers does not mutually obscure each other, as demonstrated in Fig. 3. In this figure, the coordinates of target points 1, 2, and 3 are $(r, z) = (0.1, 0.4)$ m, $(0.2, 0.2)$ m, and $(0.25, 0.65)$ m, respectively. Both numerical computations and experimental measurements yield pseudo-spectrum peaks that align with the coordinates of the target points.

It is worth noting that due to the inherent regularity in the spatial-frequency-polarization entanglement of toroidal pulses, we can achieve accurate localization using spatial pseudo-spectrum computations regardless of the type of receiver placed at the target location. As long as the receiver's operating frequency

range satisfies the frequency range used for measuring the spectrum, there is no need to employ a receiver identical to the one used in the measurement of the localization information database.

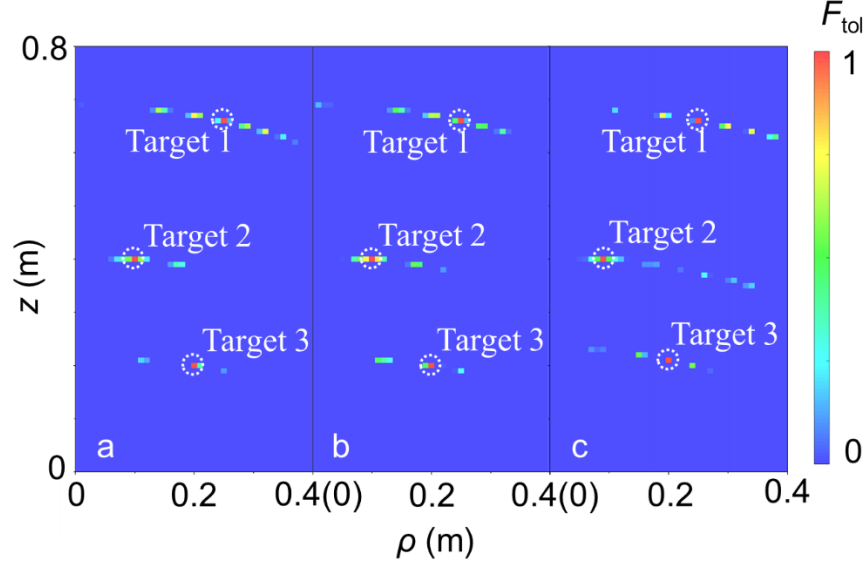


Fig. 3 Multi-target localization pseudo-spectrum based on toroidal pulses. (a) Localization pseudo-spectrum computed using ideal toroidal pulses; (b) Localization pseudo-spectrum computed using toroidal pulses with a signal-to-noise ratio of 20 dB; (c) Localization pseudo-spectrum constructed from experimental data.

Evaluation of localization accuracy. To quantitatively demonstrate the localization performance of our method, we employed the displacement metric, which quantifies the spatial deviation between the estimated localization (derived from the peak of the spatial pseudo-spectrum) and the actual target localization. Fig. 4 illustrates the displacement when targets are situated at various locations within the primary coverage area of the toroidal pulses. Due to the rotational symmetry of toroidal pulses, examining half of the cylindrical coordinate system along the z -axis suffices to capture their full spatial characteristics. In Fig. 4, the value at each (ρ_0, z_0) localization represents the displacement normalized by the shortest wavelength $\lambda_{min} = 0.03m$ (corresponding to 10GHz) used in the pseudo-spectrum computation, when the actual target localization is (ρ_0, z_0) . When utilizing ideal toroidal pulses for localization, the displacement is zero

regardless of the target's localization. When noise is introduced to the ideal toroidal pulse, the displacement remains below $0.5\lambda_{min}$ ($0.3\lambda_{cen}$ at the central frequency 6 GHz) for 91.82% of the localizations, indicating robust localization accuracy even in noisy environments. Experimental results show that 97.15% of the displacements are less than $0.5\lambda_{min}$ ($0.3\lambda_{cen}$) when targets are situated at different locations, consistent with the findings obtained using noisy toroidal pulses. From the above findings, it is evident that owing to space-time nonseparability and skyrmion topology, localization methods based on toroidal pulses can achieve ultrahigh precision in positioning, thus enabling super-resolution.

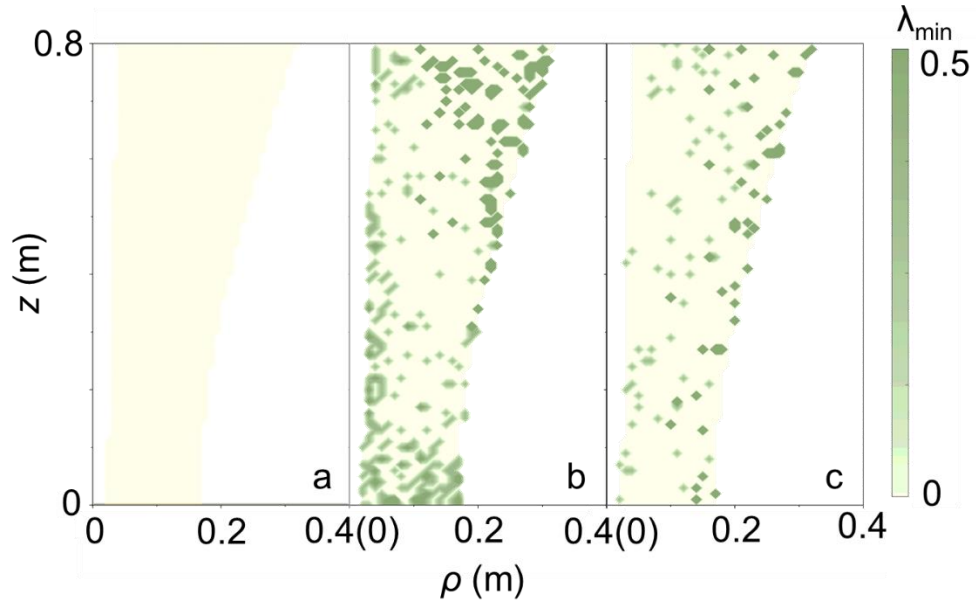


Fig. 4 Localization displacement metrics. (a) Displacement metrics computed using ideal toroidal pulses; (b) Displacement metrics computed using toroidal pulses with a signal-to-noise ratio of 20 dB; (c) Displacement metrics constructed from experimental data.

Discussion

By harnessing the inherent space-time nonseparability and skyrmion topology of toroidal pulses, we have realized precise 3D localization of receivers through the utilization of a solitary toroidal pulse transmission

antenna in free space. This method transcends the conventional spatial distance intersection principle underlying multi-transmitter localization paradigms. Our approach showcases super-resolution localization accuracy and streamlines the intricacies of localization systems.

In addition to the cooperative transmitter-receiver localization results shown in this study, the nonseparability and skyrmion topology of toroidal pulses holds promise for pioneering applications in radar detection, the internet of things, and penetrative imaging. For scattering scenarios, employing a single coaxial horn antenna to emit toroidal pulses and employing broadband dual-polarization antennas to receive scattered target echoes allows for target position determination based on echo polarization and spectral characteristics. By integrating neural network techniques with toroidal pulses, it may even be possible to reconstruct the 3D shape of targets. Radar or imaging systems based on toroidal pulses offer the potential for higher resolution with simpler system architectures and fewer transceiver units.

As a higher-order form of toroidal pulses, supertoroidal pulses exhibit more pronounced variations in spatial frequency distribution and polarization distribution [32]. Therefore, utilizing supertoroidal pulses holds promise for constructing higher-resolution positioning, detection, imaging, and other systems. Moreover, supertoroidal pulses may possess non-diffracting propagation characteristics [33], potentially enabling systems based on them to achieve greater effective detection ranges.

As classical electromagnetic waves, toroidal pulses exhibit identical propagation and topological characteristics across microwave, terahertz, and optical frequency bands. Although this paper primarily discusses the application of toroidal pulses in microwave localization systems, toroidal pulses have also been generated in the optical and terahertz frequency bands [41,42]. Hence, the methodology proposed in this paper also holds potential for applications in optical fields such as nanoscale particle metrology and super-resolution imaging.

Methods

Numerical localization method for ideal toroidal pulses. The specific implementation steps of numerical localization based on ideal toroidal pulses are as follows: (1) Generate an ideal toroidal pulse based on Eqs. (1-3) in Matlab software with $q_1=0.02\text{m}$ and $q_2=50q_1$, setting the propagation axis of the toroidal pulse as the z-axis; (2) Uniformly sample within the region of $x=[-0.4\ 0.4]\text{m}$, $y=[-0.4\ 0.4]\text{m}$, $z=[0\ 0.8]\text{m}$ with a 1cm interval, and record the spectrum of the toroidal pulse at each sampling point; (3) Assume the target is located at Position 0 (ρ_0, z_0, θ_0) , use the data recorded at Position 0 (ρ_0, z_0, θ_0) and Position 1 (ρ_1, z_1, θ_1) obtained in step (2) to calculate the pseudo-spectrum value $F_{tol}(\rho_1, z_1, \theta_1)$ at Position 1 (ρ_1, z_1, θ_1) according to Eqs. (4-8); (4) Traverse the coordinates of Position 1 throughout the entire computational domain, repeatedly perform Step (3), and obtain the pseudo-spectrum map of the entire space; (5) Identify the position $(\rho'_0, z'_0, \theta'_0)$ with the highest amplitude in the pseudo-spectrum map, which corresponds to the determined target position; (6) Calculate the distance between the determined position $(\rho'_0, z'_0, \theta'_0)$ and the actual target position (ρ_0, z_0, θ_0) , which represents the localization displacement value for the target position (ρ_0, z_0, θ_0) ; (7) Traverse the target Position 0 throughout the entire space, repeatedly perform Steps (3-6), and obtain the localization displacement value corresponding to each position in the entire space.

Numerical localization method for noisy toroidal pulses. The specific implementation steps of numerical localization in the presence of noise are as follows: (1) Follow the same procedure as in the case for ideal toroidal pulse; (2) After step (2) in the ideal toroidal pulse scenario, add two sets of random Gaussian white noise with signal-to-noise ratios of 20dB to the time-domain signals and spectra at each position, respectively referred to as pre-measured and target data sets; (3) Assume the target is located at Position 0 (ρ_0, z_0, θ_0) , use the data from Position 0 (ρ_0, z_0, θ_0) in the target data set recorded in step (2) and the data from Position 1 (ρ_1, z_1, θ_1) in the pre-measured data set according to Eqs. (4-8) to calculate the pseudo-spectrum value $F_{tol}(\rho_1, z_1, \theta_1)$ at Position 1 (ρ_1, z_1, θ_1) ; (4) Traverse the coordinates of Position 1 in the pre-measured data set throughout the entire computational domain, repeatedly perform Step (3), and obtain the pseudo-spectrum map of the entire space; (5-6) Follow the same steps as in the ideal toroidal pulse

scenario; (7) Traverse the target Position 0 throughout the entire space in the target data set, repeatedly perform Steps (3-6), and obtain the localization displacement value corresponding to each position in the entire space.

Experimental localization method. The TM toroidal pulses transmitter employed in the experimental validation of the proposed localization technology is a coaxial horn antenna proposed in Ref. [43]. The experimental setup utilized coaxial horn antennas operating within the frequency range of 1.3-10 GHz as the transmitting antennas for toroidal fields, while double-ridged waveguide horn antennas (operating within 1-18 GHz) served as the dual-polarized receiving antennas, simulating the user localizations to be localized. The geometric center of the coaxial horn antenna aperture was designated as the origin of the cylindrical coordinate system. The experimental frequency range was set to 2-10 GHz, with the spatial z -axis originated at a distance of 0.2 m from the coaxial horn antenna. Under identical experimental conditions, the spatial E_ρ distribution was measured twice using the same transmitting and receiving antennas. The amplitude and phase deviations between the two experimental datasets were found to be within 1%-2%. The experimental system was situated in a planar field measurement chamber, as depicted in Fig. 5(a), where the transmitting and receiving antennas were connected to a vector network analyzer and controlled by a computer. The double-ridged waveguide horn antenna could be moved in 3D space using a rail system, simulating various user localizations. Fig. 5(b) illustrates the cross-sectional structure of the coaxial horn antenna, where a 180° rotation along the symmetry axis reveals the complete antenna geometry. The black color represents the metal conductor, while the green color indicates a material with a dielectric constant of 1.3, serving to support the inner and outer conductors of the coaxial horn antenna. The antenna is fed through a coaxial cable connected at its base.

The procedure for obtaining experimental localization results is as follows: (1) A 2-10 GHz signal is fed into the coaxial horn toroidal field transmitter, with the central axis of the coaxial horn set as the z -axis and the aperture of the horn set at $z=0$; (2) Spectra are measured at each spatial position within the region of $x=[-0.4\ 0.4]\text{m}$, $y=[-0.4\ 0.4]\text{m}$, $z=[0\ 0.8]\text{m}$ at 1cm intervals, and recorded as the pre-measured data set; (3)

The target under test is placed at Position 0 (ρ_0, z_0, θ_0), and the spectrum is re-measured, representing the received signal spectrum when the target is located at Position 0. Using this re-measured spectrum and the data from Position 1 (ρ_1, z_1, θ_1) in the pre-measured data set, the pseudo-spectrum value $F_{tol}(\rho_1, z_1, \theta_1)$ at Position 1 (ρ_1, z_1, θ_1) is calculated according to Eqs. (4-8); (4-6) Follow the same steps as in the case of localization with noisy toroidal pulse; (7) The target under test is placed at different positions and traverses the entire space, repeating Steps (3-6) continuously to obtain the localization displacement value corresponding to each position in the entire space.

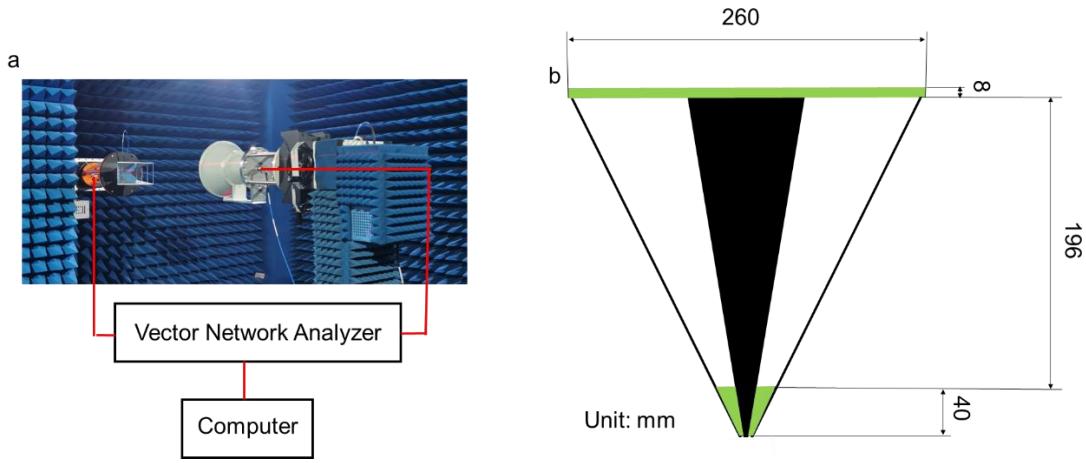


Fig. 5 (a) Experimental setup and (b) schematic of coaxial horn antenna transmitting microwave toroidal pulses. The experimental setup utilized coaxial horn antennas as the transmitting antennas for toroidal fields, while double-ridged waveguide horn antennas served as the dual-polarized receiving antennas, simulating the user localizations to be localized.

References

1. Prescott, W. H., Davis, J. L., & Svarc, J. L.. Global positioning system measurements for crustal deformation: Precision and accuracy. *Science* **244**(4910), 1337-1340 (1989).
2. Giles, J.. EU plans global positioning system. *Nature* **410**(6831), 853-853 (2001).

3. Elsheikh, M., Iqbal, U., Noureldin, A., & Korenberg, M.. The implementation of precise point positioning (PPP): a comprehensive review. *Sensors* **23**(21), 8874 (2023).
4. Kentosh, J. , & Mohageg, M. . Global positioning system test of the local position invariance of planck's constant. *Phys. Rev. Lett.* **108**(11), 110801 (2012).
5. Rizos, C., & Yang, L.. Background and recent advances in the Locata terrestrial positioning and timing technology. *Sensors* **19**(8), 1821 (2019).
6. Humphreys, T. E., Murrian, M. J., & Narula, L.. Deep-urban unaided precise global navigation satellite system vehicle positioning. *IEEE Intell. Transp. Syst. Mag.* **12**(3), 109-122 (2020).
7. Giovannetti, V. , Lloyd, S. , & Maccone, L.. Quantum-enhanced positioning and clock synchronization. *Nature* **412**(6845), 417-419 (2001).
8. del Peral-Rosado, J. A., Raulefs, R., López-Salcedo, J. A., & Seco-Granados, G.. Survey of cellular mobile radio localization methods: From 1G to 5G. *IEEE Commun. Surveys Tuts.* **20**(2), 1124-1148 (2017).
9. Janssen, T., Koppert, A., Berkvens, R., & Weyn, M.. A survey on IoT positioning leveraging LPWAN, GNSS and LEO-PNT. *IEEE Internet Things J.* **10**(13), 11135-11159, (2023).
10. Hui Chen, et al. Phone signals can help you find your way in cities even without GPS. *Nature* **611**, 454-455 (2022).
11. Koelemeij, J.C.J., Dun, H., Diouf, C.E.V. et al. A hybrid optical–wireless network for decimetre-level terrestrial positioning. *Nature* **611**, 473–478 (2022).
12. Guerra, A., Guidi, F., Dardari, D., & Djurić, P. M.. Near-field tracking with large antenna arrays: Fundamental limits and practical algorithms. *IEEE Trans. Signal Process.* **69**, 5723-5738 (2021).
13. Cohen, S. D., Cavalcante, H. L. D. S., & Gauthier, D. J.. Subwavelength position sensing using nonlinear feedback and wave chaos. *Phys. Rev. Lett.* **107**(25), 254103 (2011).
14. Faccio, D., Velten, A. & Wetzstein, G. Non-line-of-sight imaging. *Nat. Rev. Phy.* **2**, 318–327 (2020).

15. Del Hougne, P. , Imani, M. F. , Fink, M. , Smith, D. R. , & Lerosey, G. . Precise localization of multiple noncooperative objects in a disordered cavity by wave front shaping. *Phys. Rev. Lett.* **121**(6), 063901 (2018).
16. Gigan, P. del Hougne, Deeply Subwavelength Localization with Reverberation-Coded Aperture. *Phys. Rev. Lett.* **127**, 043903 (2021).
17. Nye, J. F. & Berry, M. V. Dislocations in wave trains. In *A Half-Century of Physical Asymptotics and Other Di-versions: Selected Works by Michael Berry*, 6–31 (World Scientific, 1974).
18. Willner, A. E., Pang, K., Song, H., Zou, K., & Zhou, H.. Orbital angular momentum of light for communications. *Appl. Phy. Rev.* **8**(4), 041312, (2021).
19. Berry, M. Making waves in physics. *Nature* **403**, 21–21 (2000).
20. Bliokh, K. Y., Karimi, E., et al. Roadmap on structured waves. *J. Opt.* **25**(10), 103001 (2023).
21. Wan, Z., Wang, H., Liu, Q., Fu, X., & Shen, Y.. Ultra-degree-of-freedom structured light for ultracapacity information carriers. *ACS Photonics* **10**(7), 2149-2164 (2023).
22. Wan, Z., Shen, Y., Wang, Z. et al. Divergence-degenerate spatial multiplexing towards future ultrahigh capacity, low error-rate optical communications. *Light Sci Appl.* **11**, 144 (2022).
23. Pryamikov, A. Rising complexity of the OAM beam structure as a way to a higher data capacity. *Light Sci Appl.* **11**, 221 (2022).
24. Berg-Johansen, S., Töppel, F., Stiller, B., Banzer, P., Ornigotti, M., Giacobino, E., ... & Marquardt, C.. Classically entangled optical beams for high-speed kinematic sensing. *Optica* **2**(10), 864-868 (2015).
25. Yuan, G. H., & Zheludev, N. I. Detecting nanometric displacements with optical ruler metrology. *Science* **364**(6442), 771-775 (2019).
26. Vettenburg, T., Dalgarno, H. I., Nylk, J., Coll-Lladó, C., Ferrier, D. E., Čižmár, T., ... & Dholakia, K.. Light-sheet microscopy using an Airy beam. *Nat. Methods* **11**(5), 541-544 (2014).
27. Zheludev, N. I., & Yuan, G. Optical superoscillation technologies beyond the diffraction limit. *Nat. Rev. Phys.* **4**(1), 16-32 (2022).

28. Jia, S., Vaughan, J. C., & Zhuang, X.. Isotropic three-dimensional super-resolution imaging with a self-bending point spread function. *Nat. Photonics* **8**(4), 302-306 (2014).
29. Pei Miao et al. ,Orbital angular momentum microlaser.*Science* **353**, 464-467 (2016).
30. Hellwarth, R. W., & Nouchi, P.. Focused one-cycle electromagnetic pulses. *Phy. Rev. E* **54**(1), 889 (1996).
31. Shen, Y., Zhan. Q., et al. Roadmap on spatiotemporal light fields. *J. Opt.* **25**(9), 093001 (2023).
32. Shen, Y., Hou, Y., Papasimakis, N., & Zheludev, N. I. Supertoroidal light pulses as electromagnetic skyrmions propagating in free space. *Nat. Commun.* **12**(1), 5891 (2021).
33. Shen, Y., Papasimakis, N., & Zheludev, N. I.. Nondiffracting supertoroidal pulses: optical “Kármán vortex streets”. *Nat. Commun.* (2024).
34. Kaelberer, T., Fedotov, V. A., Papasimakis, N., Tsai, D. P., & Zheludev, N. I.. Toroidal dipolar response in a metamaterial. *Science* **330**(6010), 1510-1512 (2010).
35. He, C., Shen, Y., & Forbes, A. Towards higher-dimensional structured light. *Light Sci Appl.* **11**(1) 205 (2022).
36. Shen, Y. & Rosales-Guzmán, C. Nonseparable states of light: from quantum to classical. *Laser Photon. Rev.* **16**(7), 2100533 (2022).
37. Shen, Y., Zdagkas, A., Papasimakis, N., & Zheludev, N. I. (2021). Measures of space-time nonseparability of electromagnetic pulses. *Phy. Rev. Res.* **3**(1), 013236.
38. Shen, Y., Zhang, Q., Shi, P., Du, L., Yuan, X., & Zayats, A. V.. Optical skyrmions and other topological quasiparticles of light. *Nat. Photonics* **18**(1), 15-25 (2024).
39. Papasimakis, N., Fedotov, V., Savinov, V. et al. Electromagnetic toroidal excitations in matter and free space. *Nat. Material* **15**, 263–271 (2016).
40. Raybould, T., Fedotov, V. A., Papasimakis, N., Youngs, I., & Zheludev, N. I.. Exciting dynamic anapoles with electromagnetic doughnut pulses. *Appl. Phys. Lett.* **111**(8), 081104 (2017).
41. Zdagkas, A., McDonnell, C., Deng, J., Shen, Y., Li, G., Ellenbogen, T., ... & Zheludev, N. I.. Observation of toroidal pulses of light. *Nat. Photonics* **16**(7), 523-528 (2022).

42. Jana, K., Mi, Y., Møller, S. H., Ko, D. H., Gholam-Mirzaei, S., Abdollahpour, D., ... & Corkum, P. B.. Quantum control of flying doughnut terahertz pulses. *Sci. Adv.* **10**(2), eadl1803 (2024).
43. Wang, R., Hu, Z. Q., Bao, P. Y., Shi, S., Wang, B. Z., Zheludev, N. I., & Shen, Y.. Free-space propagation and skyrmion topology of toroidal electromagnetic pulses. arXiv preprint arXiv:2311.01765 (2023).
44. Powell, S. B., Garnett, R., Marshall, J., Rizk, C., & Gruev, V. Bioinspired polarization vision enables underwater geolocalization. *Sci. Adv.* **4**(4), eaao6841 (2018).
45. Graydon, O.. Global position by polarization. *Nat. Photonics* **12**(6), 318-318 (2018).

Acknowledgements

The authors acknowledge the supports of the the National Natural Science Foundation of China (62171081, 61901086, U2341207), the Aeronautical Science Foundation of China (2023Z062080002), and the Natural Science Foundation of Sichuan Province (2022NSFSC0039). Y. Shen also acknowledges the support from Nanyang Technological University Start Up Grant, Singapore Ministry of Education (MOE) AcRF Tier 1 grant (RG157/23), and MoE AcRF Tier 1 Thematic grant (RT11/23).

Contributions

R.W. conceived the ideas and supervised the project, R.W. and P.Y.B. performed the theoretical modeling and numerical simulations, R.W. developed the experimental methods, P.Y.B., Z.Q.H. and R.W. conducted the experimental measurements, R.W., P.Y.B. and Y.S. conducted data analysis. All authors wrote the manuscript and participated the discussions.

Competing interests

The authors declare no competing interests.

Data and materials availability

The data that support the findings of this study are available from the corresponding author upon reasonable request.

Additional information

Supplementary information is available for this paper. Correspondence and requests for materials should be addressed to R.W. and Y.S..